Research Article

Numerical Modelling of Field Test for Crack Risk Assessment of Early Age Concrete Containing Fly Ash

G. M. Ji [ID],[1] **T. Kanstad** [ID],[2] **and Ø. Bjøntegaard**[3]

[1]*SINTEF Ocean, 7450 Trondheim, Norway*
[2]*The Norwegian University of Science and Technology (NTNU), 7491 Trondheim, Norway*
[3]*Norwegian Public Roads Administration, Tunnel and Concrete Section, Norway*

Correspondence should be addressed to T. Kanstad; terje.kanstad@ntnu.no

The high-strength/high-performance concretes are prone to cracking at early age due to low water/binder ratio. The replacement of cement with mineral additives such as fly ash and blast-furnace slag reduces the hydration heat during the hardening phase, but at the same time, it has significant influence on the development of mechanic and viscoelastic properties of early age concrete. Its potential benefit to minimize the cracking risk was investigated through a filed experiment carried out by the Norwegian Directorate of Roads. The temperature development and strain development of the early age concrete with/without the fly ash were measured for a "double-wall" structure. Based on experimental data and well-documented material models which were verified by calibration of restraint stress development in TSTM test, thermal-structural analysis was performed by finite element program DIANA to assess the cracking risk for concrete structures during hardening. The calculated and measured temperature and strain in the structure had good agreement, and the analysis results showed that mineral additives such as flay ash are beneficial in reducing cracking risk for young concrete. Furthermore, parameter studies were performed to investigate the influence of the two major factors: creep and volume change (autogenous shrinkage and thermal dilation) during hardening, on the stress development in the structure.

1. Introduction

Prediction of early age cracking is traditionally based on temperature criteria. The temperature development in the young concrete is then calculated and cracking tendency is deduced from the maximal temperature difference in a structure. To avoid cracking, limitations were applied to maximum temperature, temperature difference between the surface and the center of the structure, and between the new and the older adjoining structures. These limitations were based on practical experience and experience from the laboratory [1].

The main drawback of the temperature-based crack risk estimation is that the other involving factors are not considered: restraint conditions and several other material properties. Many researchers [2–4] have shown that there is no general correlation between stress and temperature. Whether young concrete will crack or not, it depends very much on restraint conditions and material properties.

For reliable crack prediction at early ages, strain criteria must be applied, and this calls for well-documented material models. In recent years, an increased interest in cracking of hardening concrete has led to extensive research on this subject. Making reliable cracking risk assessments involves experimental testing and advanced modelling of the time and temperature-dependent behavior of the properties, the restraint conditions of the structure, and the external environmental conditions. A large number of material models for young concrete have been presented and implemented in computer programs for the simulation of stress development [5–9]. Based on extensive experimental test, the well-documented material models were proposed, and verification of the development of the restraint stress in the TSTM test showed that the combination of the material models is capable to describe the total behavior of hardening concrete [10, 11].

Mineral additives such as silica fume (SF), blast-furnace slag (BFS), and fly ash (FA) have been used extensively in

production of high-performance concrete in the last decades, and the influences of fly ash on various properties of early age concrete were investigated extensively in [11]. The potential benefit to minimize the cracking risk by replacement of cement with FA was investigated through a field experiment in the current study. Temperature and strain developments in 26 different positions were measured in two different sections of the "double-wall" structure with one wall of SV40 concrete and another of low-heat concrete. Advanced thermal and structural analyses were then performed by finite element program DIANA [12], and the simulation results were compared with the test results.

2. Methodology of Thermal and Structural Analysis

The thermal and structure problems are solved in sequence. Concrete is treated as a homogeneous material in simulation; therefore, the calculated stresses are not representative for, e.g., the boundary zones around aggregate but represent only regions with a size larger than some characteristic dimensions, e.g., the maximum aggregate size. The procedures to solve the thermal and structural problems are described in following section.

2.1. Solution of the Thermal Problem. Transient thermal analysis is used to calculate the temperature field. The general theory to solve the thermal problem is well established and described in many researches [3, 6, 13–16]. The finite element equations of the thermal problem are formulated using the Galerkin weighting procedure, and the procedure extends the equilibrium to a finite volume. In the finite element method, the structure is divided into discrete element, and the temperature field and the temperature gradient are approximated as the linear function of the nodal temperature. The temperature gradient depends on the total quantity of hydration heat, boundary conditions, thermal properties, and discontinuity in geometry and material properties [14].

2.2. Solution of the Mechanical Problem. The nonlinear finite element analysis is used to calculate the stress development, and the theory is described in [14]. The starting point for numerical analysis of the development of stresses in time is the incremental formulation of the principle of virtual work. The displacements are approximated by interpolation of the nodal displacement. The constitutive relation for aging viscoelastic material is given via creep compliance or relaxation compliance and can be solved by integral or differential formulation [14]:

$$\varepsilon(t) = \int_{t_0}^{t} J(t, t') \overline{C} \, d\sigma(t') + \varepsilon^0(t),$$

$$\sigma(t) = \int_{t_0}^{t} R(t, t') \overline{D} \, d\varepsilon(t') + \sigma^0(t), \tag{1}$$

where $\overline{C}$ and $\overline{D}$ are the dimensionless matrix that relate the three-dimensional deformation state to the one-dimensional creep or relaxation function by using Poisson's ratio v:

$$\overline{C} = \begin{bmatrix} 1 & -v & -v & 0 & 0 & 0 \\ -v & 1 & -v & 0 & 0 & 0 \\ -v & -v & 1 & 0 & 0 & 0 \\ 0 & 0 & 0 & 2(1+v) & 0 & 0 \\ 0 & 0 & 0 & 0 & 2(1+v) & 0 \\ 0 & 0 & 0 & 0 & 0 & 2(1+v) \end{bmatrix}, \tag{2}$$

$$\overline{D} = \overline{C}^{-1}.$$

The stress gradient depends on temperature distribution, mechanical properties, restraint conditions, discontinuity in geometry, and material properties. In the thermal stress analysis, the element model must permit the same level of complexity for the strain field as that for the temperature field. Since the stresses are less accurate than displacements and temperatures, stress calculations need finer mesh than temperature calculations, and the order of the element in stress analysis has to be of higher order than the element in temperature analysis. If the same element model is used in both analyses, the requirements of stress analysis are usually decisive [14].

3. Field Test

Within the NOR-CRACK project, a great deal of R&D work was carried out by the Norwegian Public Roads Administration to develop a low-heat concrete with a minimal risk of early age cracking. In order to evaluate the crack risk of the low-heat concrete, a field investigation on a specially designed structure with relevant dimensions was carried out in Norway. It was essential to compare the cracking risk of low-heat concrete with that of SV40 concrete which is commonly used in Norway. The composition of SV40 and low-heat concretes is shown in Table 1.

The double-wall structure was tested in the field—one wall for each type of concrete and the slab with SV40. The dimension of the bottom slab is $5.4 \times 15 \times 0.8$ m, and the slab was about 2½ weeks old when both walls were cast at the same time. The dimension of the double wall is $1.0 \times 15 \times 2.0$ m as shown in Figure 1 [17].

A total of 26 strain gauges of the vibrating-wire type (GEOKON VCE-4200) were installed prior to casting. These strain gauges measure simultaneously both temperature and strain in the same position. Hence, concrete strains can be calculated by compensating strain due to temperature. 24 strain gauges were installed in the longitudinal direction at two sections of the structure—5.0 and 7.5 meters from the end. For each section, 4 gauges were installed in each wall (8 in total) and 2 gauges under each wall (4 in total in the slab), as shown in Figure 2. In addition, for each wall, one strain gauge was installed transversely 0.75 m from the end of the structure to measure the approximated free-deformation strains.

The bottom slab was first casted, and after 2 weeks, the casting of both sides of walls was started simultaneously in the middle of the day. The air temperature was measured by a Temperature Data Logger and Recorder continuously when the casting of the walls started, and the recorded

TABLE 1: Concrete composition, all values in kg/m³.

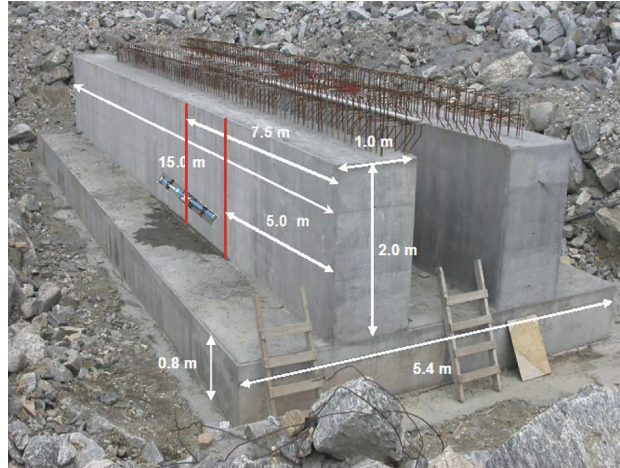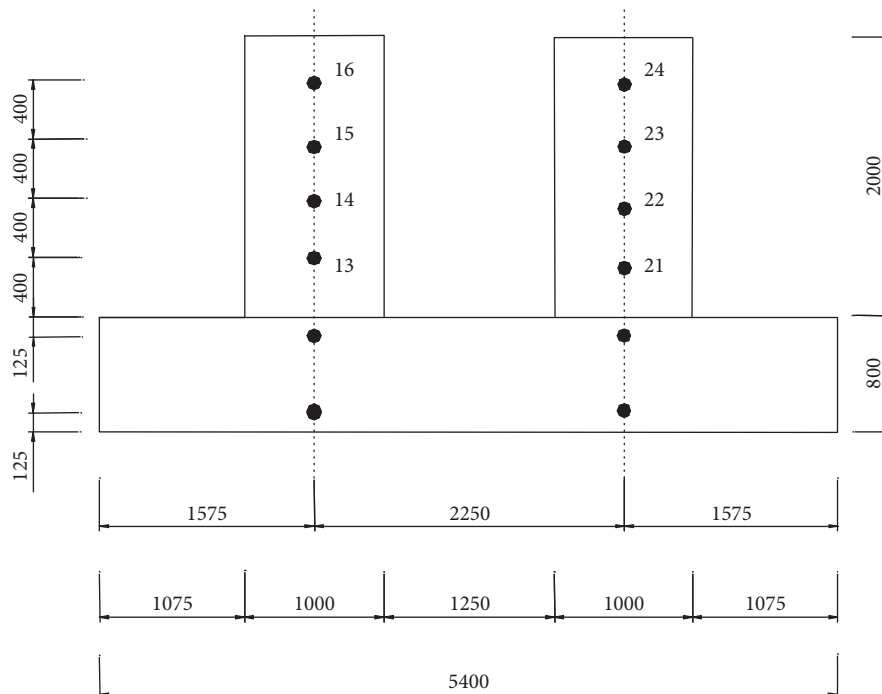| Concrete	OPC (Norcem Anleggsement)	Fly ash	Silica fume	Coarse aggregate (8–16 mm)	Fine aggregate (0–8 mm)	Total water
SV40	404	—	20	880	910	178
Low-heat	233	140	12	879	899	178

FIGURE 1: Field test.

FIGURE 2: Middle cross section of the double-wall structure and the positions of the strain gauges (black dots) (dimensions in mm).

dry-bulb temperature is shown in Figure 3. The concretes were blended at site, and the fresh concrete temperature for the "low-heat" concrete was about 23.0°C and for "SV40" about 21.5°C. After casting of the walls was finished in the evening, the plastic foil was used to cover the top of the walls, and no other special curing measurements were taken during the hardening phase. The formworks on the side of the walls were removed 216 hours (9 days) after casting.

4. 3D Finite Element Model of "Double-Wall" Structure

The subgrade reaction modulus method is used to model the deformability of the ground. The modulus of the subgrade reaction is in the range of 64–128 MN/m³ for dense sand and is lager than 500 MN/m³ for rock [18]. In the analysis, the value of the vertical modulus of the subgrade reaction is set
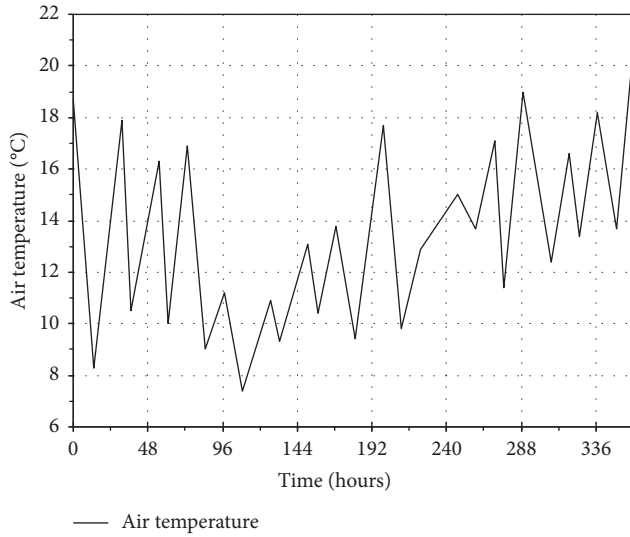
Figure 3: Temperature history of ambient air.

to $k_v = 250$ MN/m^3 for compression, $k_v = 0$ MN/m^3 for tension, and the horizontal modulus of the subgrade reaction is set to $k_h = 60$ MN/m^3.

The wind velocity reported from local weather forecast is varied between 0 and 2 m/s, and the following convection coefficients are used in the analysis before and after plastic foil and formwork were removed:

(a) Concrete-plastic foil-air convection coefficient = 0.0040 kJ/°C m^2 s

(b) Concrete-formwork-air convection coefficient = 0.0026 kJ/°C m^2 s

(c) Concrete-air convection coefficient = 0.0133 kJ/°C m^2 s

The finite element mesh of the structure used in the program Diana is shown in Figure 4, and the spring representing the vertical and horizontal moduli of the subgrade reaction is not shown in Figure 4. The 20-node isoparametric solid brick element CHX60 is used to model the concrete, and it is based on quadratic interpolation and Gauss integration. The strain ε_{xx} and stress σ_{xx} vary linearly in the x direction and quadratically in the y and z directions. The strain ε_{yy} and stress σ_{yy} vary linearly in the y direction and quadratically in the x and z directions. The strain ε_{zz} and stress σ_{zz} vary linearly in the z direction and quadratically in the x and y directions. By default, DIANA applies a $3 \times 3 \times 3$ integration scheme. The 20-node element is automatically converted to 8-node isoparametric brick element HX8HT in the heat analysis, and by default, DIANA applies a $2 \times 2 \times 2$ integration scheme for HX8HT element. The 4-node isoparametric quadrilateral element BQ4HT is used to model the boundary conditions in the thermal analysis, and by default, DIANA applies a 2×2 integration scheme [12].

The following material properties which are the main factors in assessment of cracking risk for early age concrete were calibrated in [11] and were used in current analysis:

4.1. Heat of Hydration.

The heat production is described by the approach based on the hydration degree (equivalent to maturity age) [19]:

$$Q = Q_\infty \left\{ \exp\left[-\left(\frac{\tau}{t_{eq}}\right)^\alpha \right] \right\}, \qquad (3)$$

where Q_∞, τ, and α are the model parameters that can be determined from the adiabatic temperature curve derived from semiadiabatic measurements of the heat of hydration. The thermal properties of SV40 and low-heat concretes are presented in Table 2.

4.2. Volume Change (Autogenous Shrinkage (AS) and Thermal Dilation (TD)).

The total deformation measured in the dilation rig under 60°C series was used as input for SV40 concrete, and the separation of AS and TD is calculated by the constant coefficient of thermal expansion (CTE) of 8.5×10^{-6}. The total deformation measured in the dilation rig under 45°C series was used as input for low-heat concrete, and the AS and TD are also separated by the constant CTE of 8.5×10^{-6}. The test data from the dilation rig for both concretes were presented in [11]. The effect of different ways to separate AS and TD is discussed in the parameter study.

4.3. Mechanical Properties (E-Modulus, Compressive Strength, and Tensile Strength).

The modified version of CEB-FIP MC 1990 is used to describe the development of the compressive strength, tensile strength, and modulus of elasticity, and t_0 is introduced in the equations to identify the start of significant mechanical properties development, Kanstad et al. [20, 21]:

$$f_c = f_{c28} \left\{ \exp\left[s\left(1 - \sqrt{\frac{28}{t_{eq} - t_0}} \right) \right] \right\},$$

$$f_t = f_{t28} \left\{ \exp\left[s\left(1 - \sqrt{\frac{28}{t_{eq} - t_0}} \right) \right] \right\}^{n_t}, \qquad (4)$$

$$E_c = E_{c28} \left\{ \exp\left[s\left(1 - \sqrt{\frac{28}{t_{eq} - t_0}} \right) \right] \right\}^{n_E},$$

where t_{eq} is the equivalent time, t_0 is the concrete age when the stiffness starts to increase from zero, and s is the curve fitting parameter which is determined from compressive strength development, while n_t and n_E are the curve fitting parameters dedicated for the development of the tensile strength and the elastic Young's modulus. The mechanical properties are presented in Table 3.

4.4. Creep/Relaxation Properties.

The double power law is used to model the creep behavior in the numerical simulations, and the compliance function becomes [10, 14, 22, 24] as follows:

$$J(t, t') = \frac{1}{E(t'_e)} \left(1 + \varphi \cdot (t')^{-d} (t - t')^p \right), \qquad (5)$$
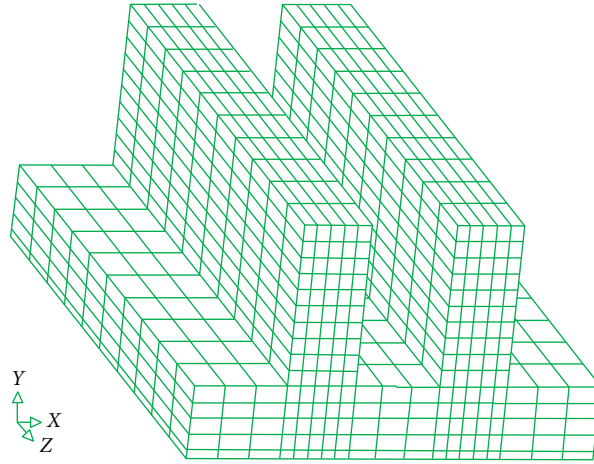
FIGURE 4: Finite element model of the double-wall structure.

TABLE 2: Thermal properties of SV40 and low-heat concretes.

Concrete	Q_∞ (kJ/kg cem)	τ	α	Thermal expansion coefficient (10^{-6}/°C)	Arrhenius constant (K)	Thermal conductivity (kJ/°C ms)	Thermal capacitance (kJ/° Cm^3)
SV40	319	15.04	1.34	10.54	2645.7	0.0026	2512.2
Low-heat	290	17.75	1.20	8.35	4353.1	0.0026	2482.4

TABLE 3: Mechanical properties of the "SV40" and "low-heat" concretes.

Concrete	f_c (28) (MPa)	f_t (28) (MPa)	E_c (28) (GPa)	s	n_t	n_E	t_0 (h)
SV40	65.11	3.86	31700	0.197	0.722	0.421	8.0
Low-heat	41.20	3.20	33360	0.418	0.561	0.251	10.5

where t is the concrete age; t' is the concrete age at loading; $E(t'_e)$ is the E modulus at the loading age; and φ, d, and p are the creep model parameters. The creep parameters for SV40 and low-heat concretes are presented in Table 4. The effect of creep/relaxation properties on the stress development is discussed in the parameter study.

5. Field Test Results

The temperature was measured at the middle section of both walls: points 13–16 for the "SV40" and points 21–24 for the "low-heat" concrete. The measured temperatures in SV40 and low-heat concretes are shown in Figures 5 and 6, respectively. Although the temperature recording was stopped for low-heat concrete at around 200 hours after casting, the collected field data are sufficient for the comparison to the numerical simulation, and the temperature of concretes will be close to the air temperature at the end.

The strain was measured at the middle section for "SV40" concrete (points 13–16) and 5.0 m section of low-heat concrete (points 17–20). The measured strains are shown in Figures 7 and 8 for SV40 and low-heat concretes, respectively. Some difficulties were experienced in the recording, and the measurements in points 17, 18, 19, and 20 failed at about 6 days, and the comparison between numerical simulation and test data could only be performed for the first 150 hours for low-heat concrete.

TABLE 4: Creep parameters for SV40 and low-heat concretes.

Concrete	d	p	φ
"SV40"	0.18	0.18	1.10
"Low-heat"	0.22	0.26	1.60

6. Numerical Analysis Results

6.1. Temperature Development. The temperature contour in the middle section of the wall at time around 32 hours after casting is shown in Figure 9, and the measured and predicted temperature developments at the middle section are shown in Figures 10 and 11. The predicted temperature developments have good agreement with the test results. The deviation of the predicted and measured maximum temperature is in the range of ±1.5°C for both the SV40 and the low-heat concretes, and the maximum difference between predicted and measured temperature during the first 2 weeks is about 3°C. The maximum temperatures in both concretes are presented in Table 5.

6.2. Strain Development. The simulated and measured total strain developments in the middle section of the SV40 wall and in the 5.0 m section of the low-heat concrete are shown in Figures 12 and 13, respectively. In the SV40 concrete wall, the calculated strain is underestimated for the lowest point (point 13, 0.4 m above the slab) with a maximum deviation
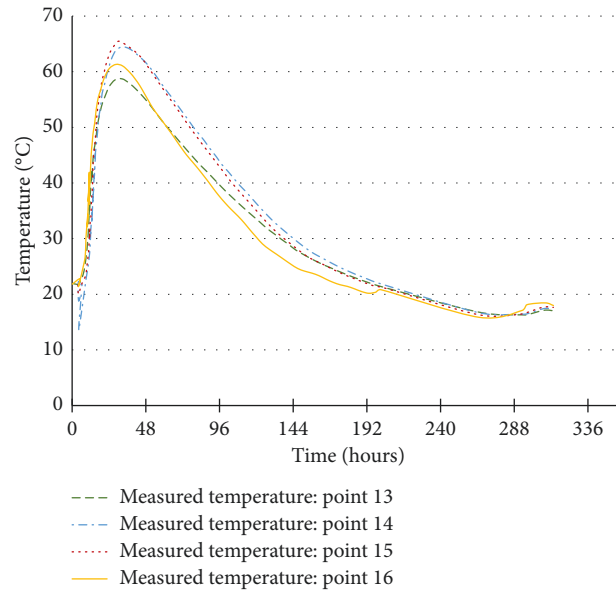
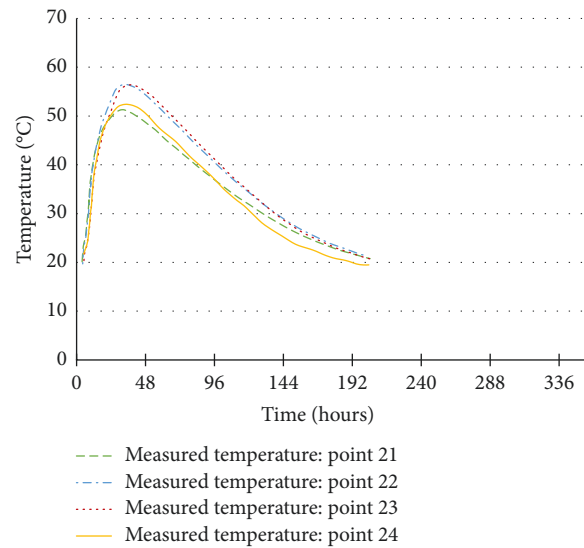Figure 5: Measured temperature in the middle section (SV40).

Figure 6: Measured temperature in the middle section (low-heat concrete).

of about 50 μ. They are in good agreement with the measured strains for the two middle points (points 14 and 15), and it is overestimated for the top point (point 16, 1.6 m above the slab) with a maximum deviation of about 100 μ. The measured strain developments of the four points at the middle section are similar, and it indicates that the rotation of the middle section is quite small. In simulation, the wall structure can slip in the horizontal direction, and vertical contact force becomes zero when the bottom slab is uplifted from soil foundation. Stress analysis in next section showed that the maximum stresses occur at the area around the two middle points, and then it is most important to have reliable both test and simulation results at the middle points.

In the low-heat concrete wall, the calculated strains of the bottom three points (points 17, 18, and 19) agree well with the measured ones for first 150 hours, and only the calculated strain of the top point (point 20) is higher than the measured one about 50 μ.

6.3. Stress Development.

The stress contour plot is shown in Figure 14, and it shows that the maximum stress occurs at the locations which are different from the locations of maximum temperature as shown in Figure 9. The maximum stress occurs at the lower part of the middle of both walls. The comparisons between stress and tensile strength developments are shown in Figure 15 for SV40 and low-heat concretes, respectively. The crack index, defined as the ratio between tensile stress $\sigma(t)$ and tensile strength $f(t)$, has also been determined, and it is shown in Figure 16. The maximum stress and corresponding cracking index in both concretes are presented in Table 6. The maximum crack
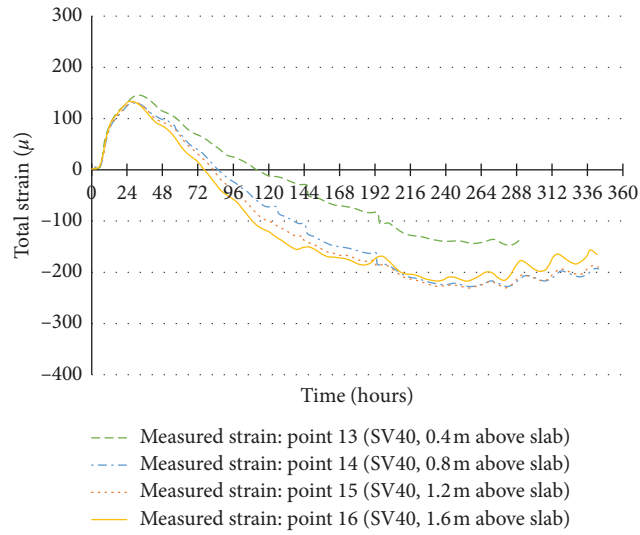
Figure 7: Measured total strain development in the middle section of the SV40 wall.
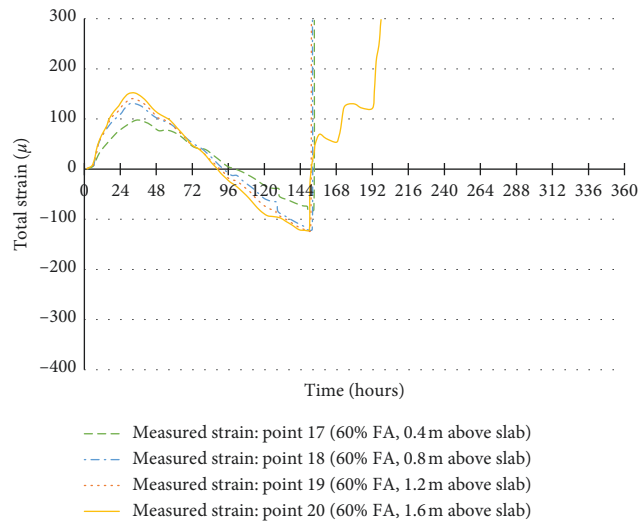

Figure 8: Measured total strain development in the 5.0 m section of low-heat concrete.
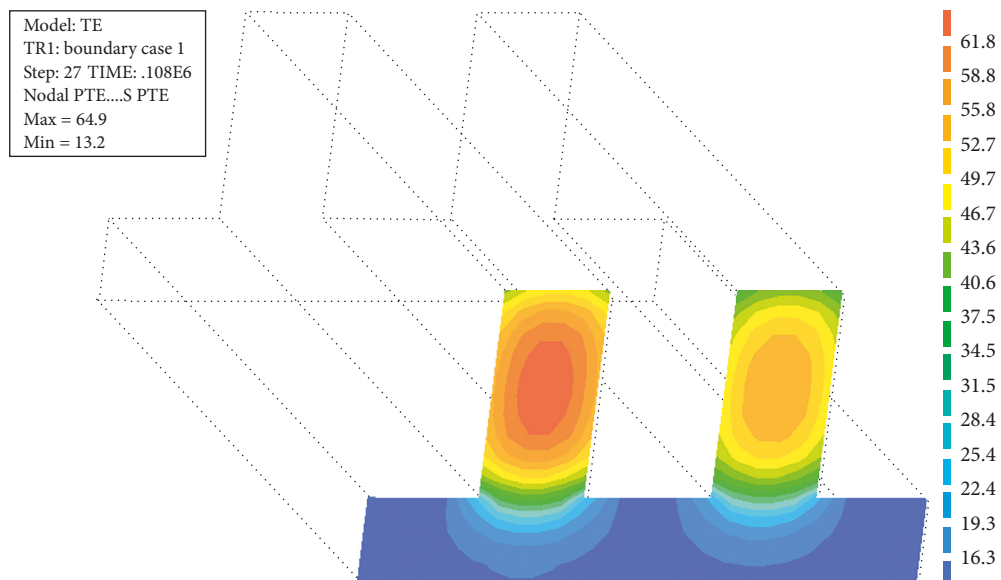

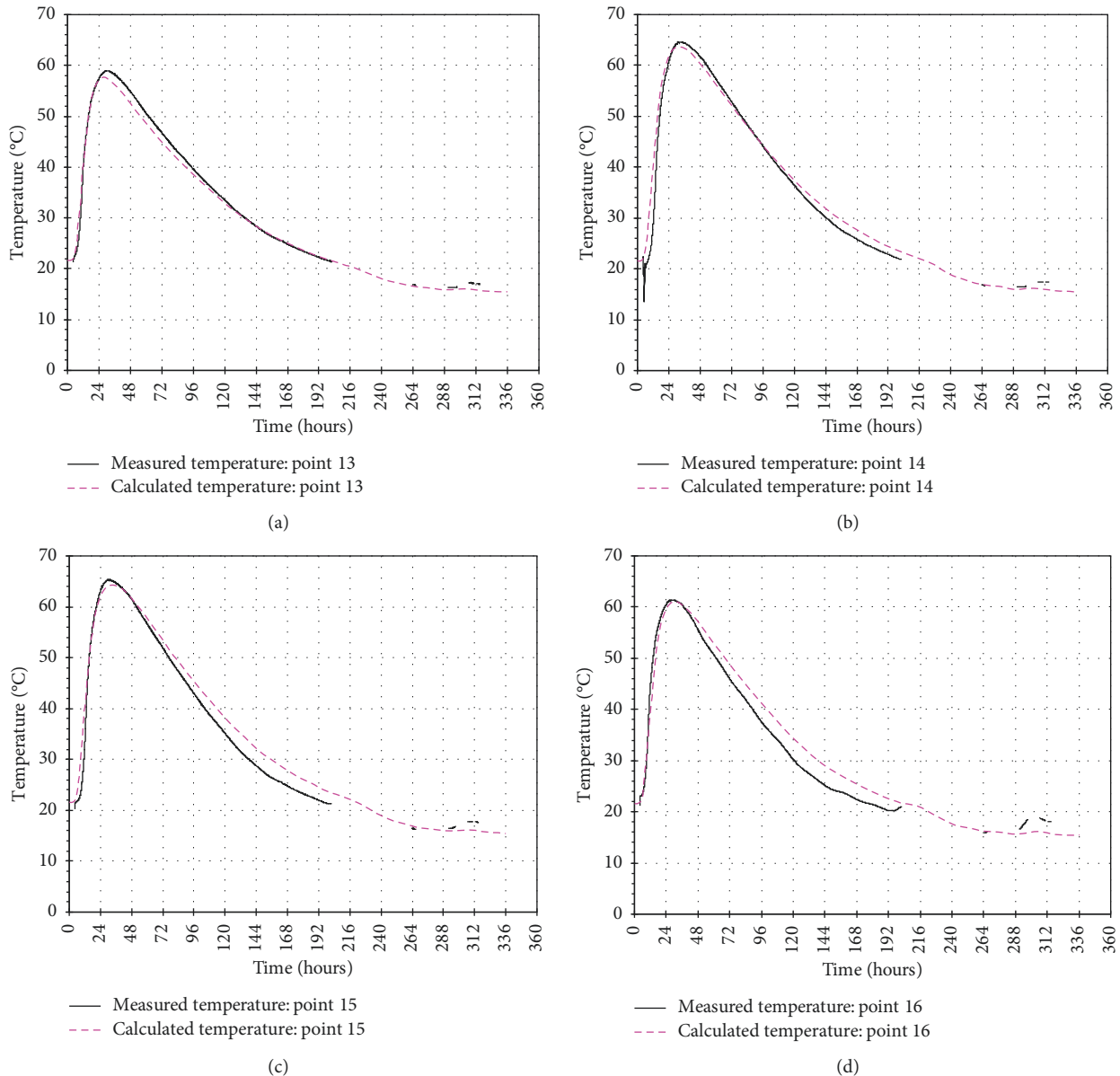Figure 9: Temperature contour in the middle section of the wall.

Figure 10: Calculated and measured temperatures in the middle section (SV40).

indexes are about 0.97 and 0.75 for SV40 and low-heat concretes, respectively.

Cracks are observed in the SV40 wall after the removal of the formwork, and according to the strain measurements shown in Figure 12, they probably appeared around 7 and 9 days after casting, and the crack increased the strain in the two lower points (points 13 and 14). The minor cracks were also observed in the low-heat concrete, but the cracking in SV40 concrete was more severe than the cracking in low-heat concrete.

7. Parameter Study

7.1. Creep Property. Creep is a very import factor which leads to reduction of the restraint stresses in the order of 40–50% compared to the elastic case without creep, and creep data during the whole period of hardening (heating and cooling) are necessary for reliable prediction of cracking risk [23, 24]. The effect of creep was investigated quantitively by variation of the parameter φ in creep compliance in the current study.

The restraint stress in the double-wall structure was calculated when only the parameter φ in creep compliance is increased or decreased by 50% as shown in Figure 17 and Table 7. It can be seen from Figure 18 that 50% increase of parameter φ in creep compliance leads to 15% and 20% decrease in the restraint stress for SV40 and low-heat concretes, respectively. Higher creep in the early period reduces compressive stresses and consequently increases the tensile stress, while increased creep in the cooling period reduces tensile stresses. These two effects are competing, and the final effect is their summation. The 50% decrease of parameter φ in
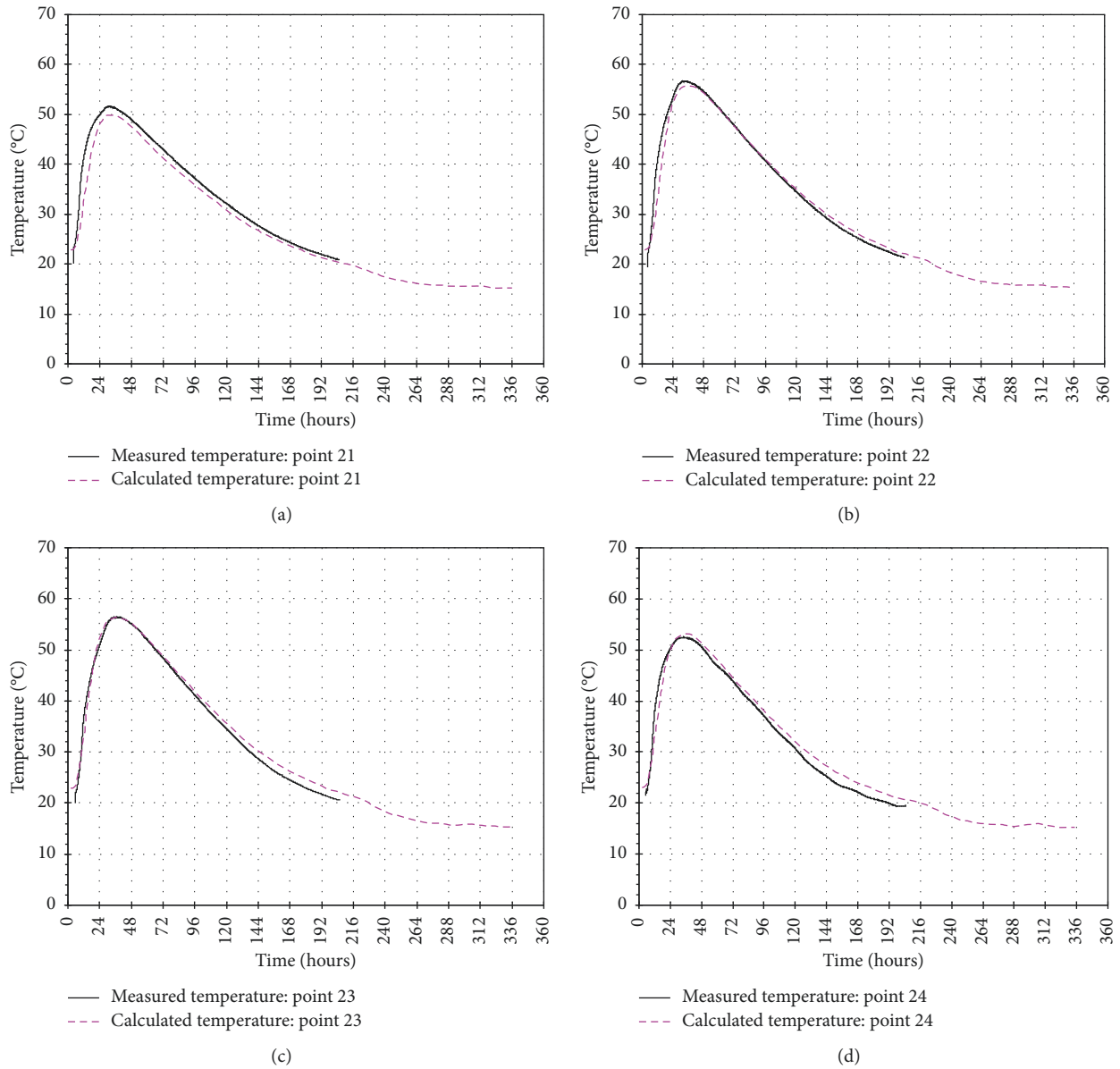
(a)

(b)

(c)

(d)

FIGURE 11: Calculated and measured temperatures in the middle section (low-heat concrete).
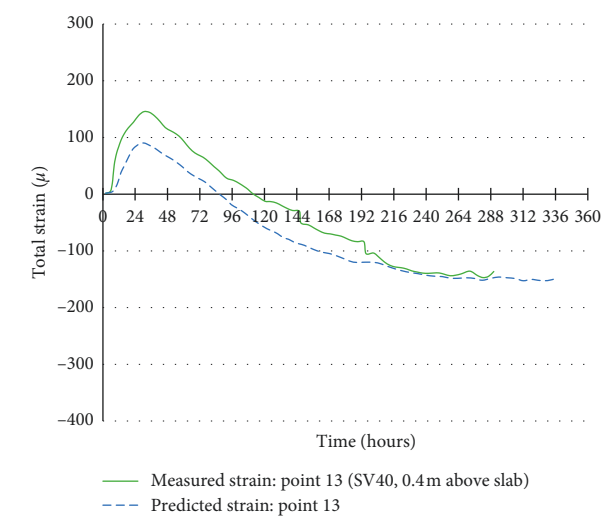
TABLE 5: Maximum temperature in concrete.

Concrete	Calculated maximum temperature (°C)	Measured maximum temperature (°C)
SV40	64.16	65.25
Low-heat	56.40	56.47

creep compliance has more influence on the stress development and leads to 26% and 30% increase in the restraint stress for SV40 and low-heat concretes, respectively. Due to the higher creep compliance, the "low-heat" concrete is more sensitive to the creep increase/decrease.

7.2. Thermal Dilation (TD) and Autogenous Shrinkage (AS).
The numerical simulation usually requires the separated input of autogenous shrinkage and thermal dilation. There

are two strategies investigated which were often used to obtain separated AS and TD under variable temperature and validation of those two strategies [25], and the applicability of both strategies is further discussed in the current study for SV40 concrete. An improved procedure is proposed on how to apply the dilation rig and TSTM test data under variable temperature histories in the numerical simulation to achieve more reliable simulation results.
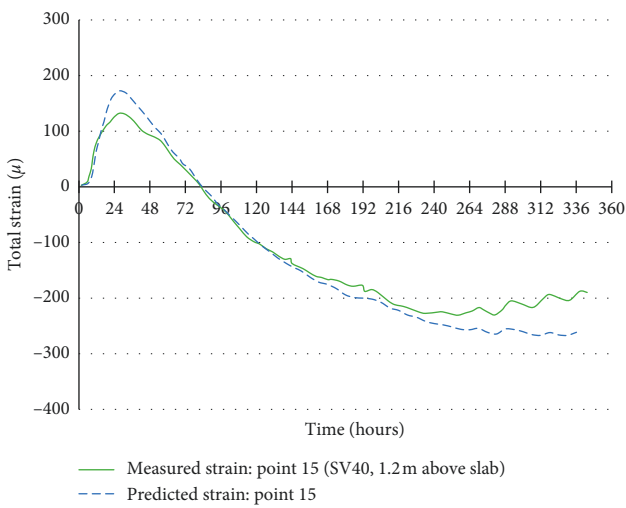
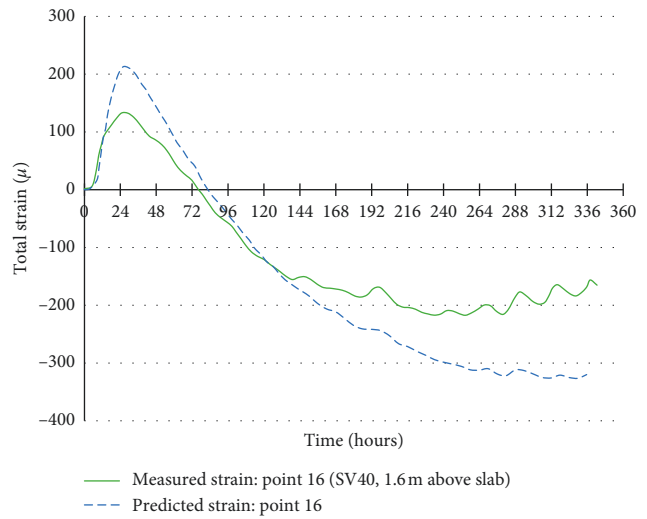For the first strategy, only autogenous shrinkage under 20°C isothermal conditions was measured, and then it was
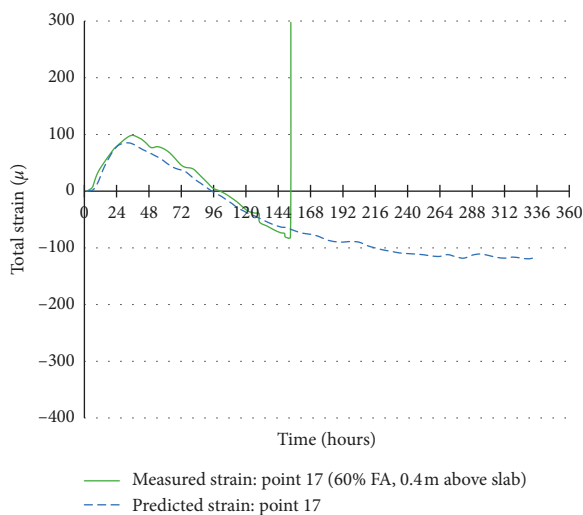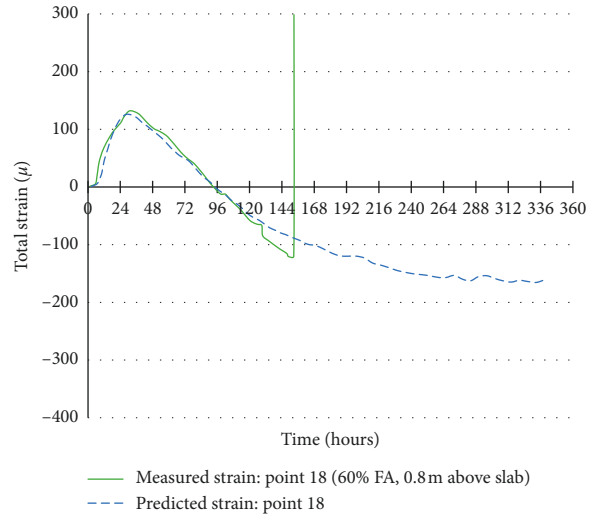
Measured strain: point 13 (SV40, 0.4 m above slab)
Predicted strain: point 13

(a)

Measured strain: point 14 (SV40, 0.8 m above slab)
Predicted strain: point 14

(b)

Measured strain: point 15 (SV40, 1.2 m above slab)
Predicted strain: point 15

(c)

Measured strain: point 16 (SV40, 1.6 m above slab)
Predicted strain: point 16
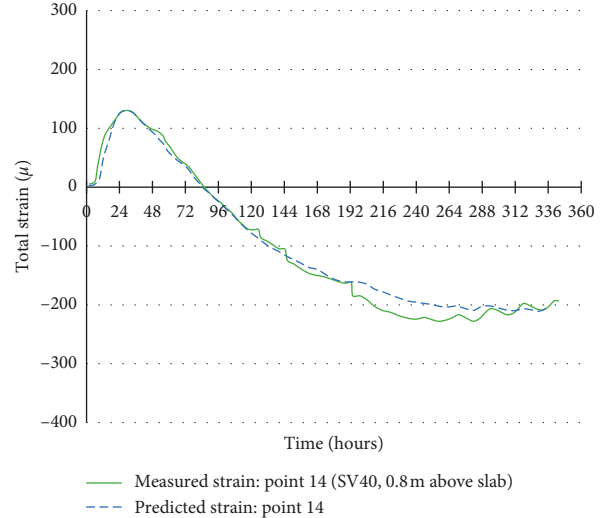
(d)

Figure 12: Simulated and measured total strain developments in the middle section of the SV40 wall.

Measured strain: point 17 (60% FA, 0.4 m above slab)
Predicted strain: point 17

(a)

Measured strain: point 18 (60% FA, 0.8 m above slab)
Predicted strain: point 18

(b)

Figure 13: Continued.

Measured strain: point 19 (60% FA, 1.2 m above slab)
--- Predicted strain: point 19

(c)

Measured strain: point 20 (60% FA, 1.6 m above slab)
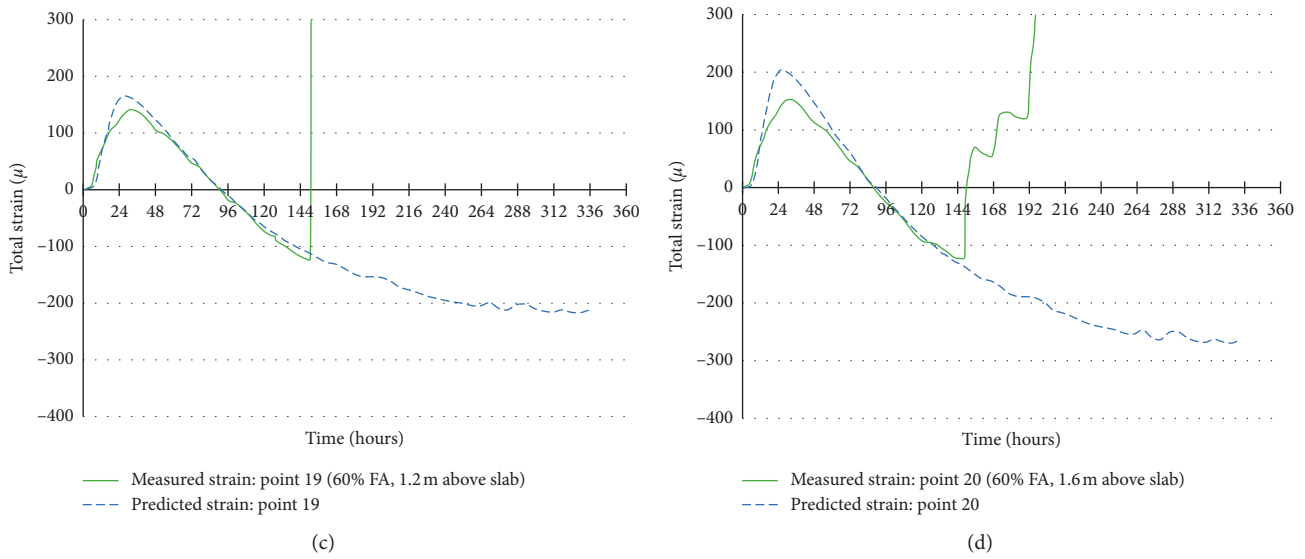--- Predicted strain: point 20

(d)

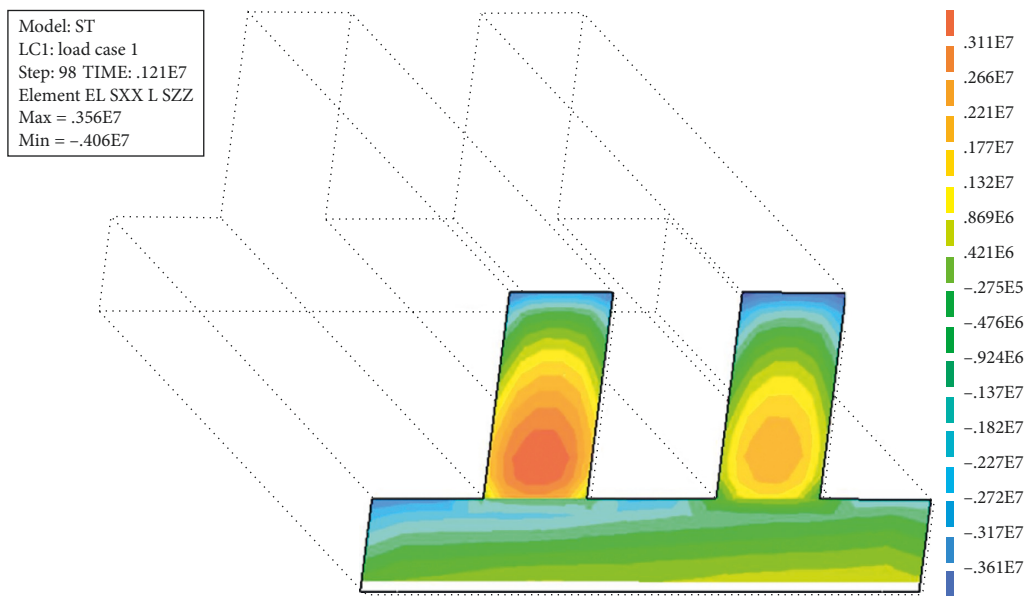Figure 13: Simulated and measured total strain developments in the 5.0 m section of the low-heat concrete.

Figure 14: Stress contour in the middle section of wall.

transferred to the autogenous shrinkage under variable temperature history by maturity concept. At the same time, the coefficient of thermal expansion (CTE) measured from harden concrete was used to calculate thermal dilation. The total deformation under variable temperature was not obtained directly from the test but from combined autogenous shrinkage and thermal dilation.

In the current study, two total deformations were calculated for SV40 concrete by transferred autogenous shrinkage combined with two constant CTEs: 8.5×10^{-6} or $10.0 \times 10^{-6}/°C$. The stress developments under those two total deformations were compared with the stress development calculated with input of measured total deformation from the TSTM test with $T_{\max} = 60°C$ (60°C series).

As shown in Figure 19, the total deformations with two different constant CTEs were different from the measured total deformation, and consequently, the calculated stress developments in those two cases could not represent the stress development in the structure. It means that only measuring autogenous shrinkage under the isothermal condition is not sufficient, and with the assumed constant CTE, it cannot ensure that the input of total deformation represents the total deformation under realistic temperature history.

According to the second strategy, the total deformation is measured in the dilation rig test under realistic temperature histories, and then it is separated to AS and TD by assumed constant CTEs.
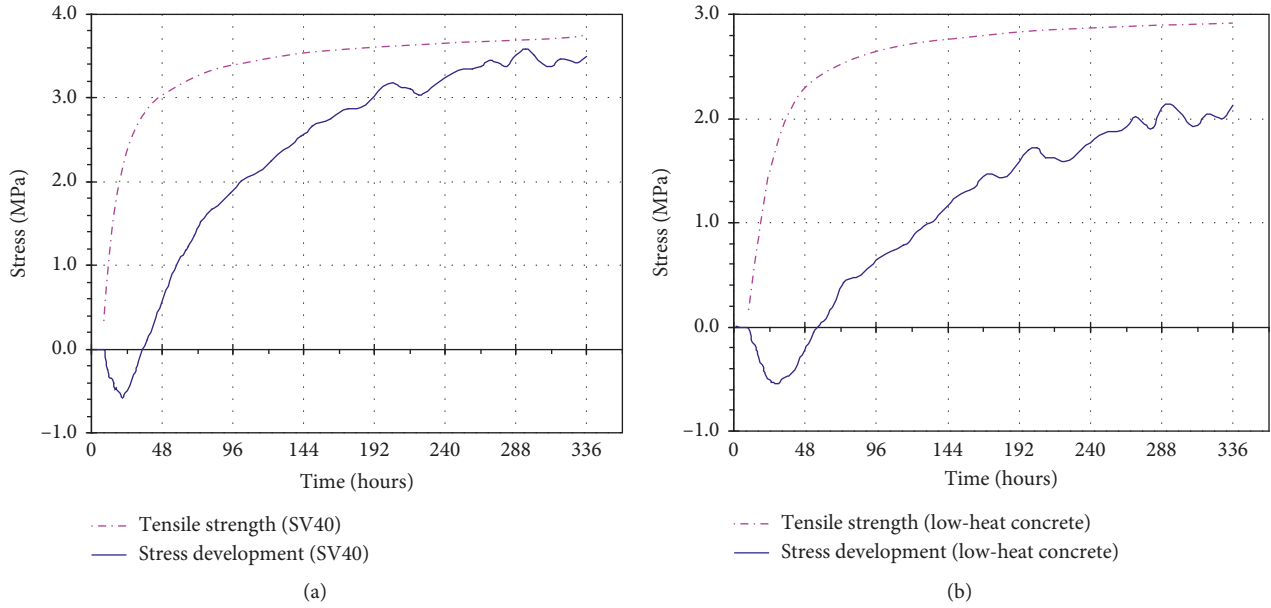
(a)

(b)

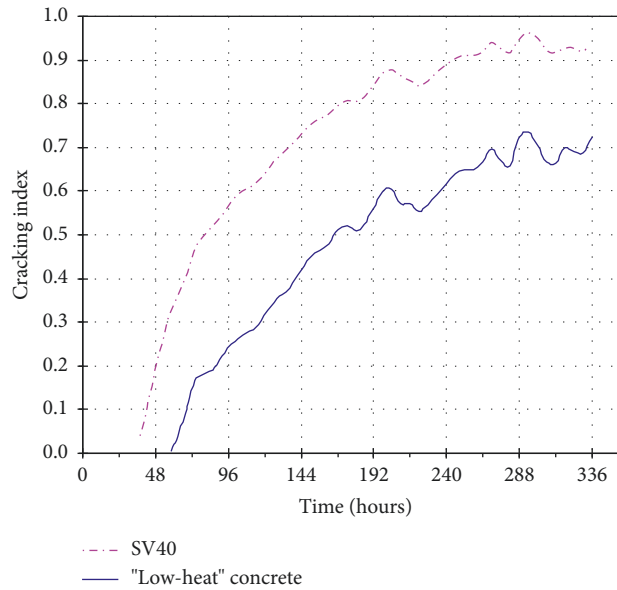FIGURE 15: Stress and tensile strength developments in (a) SV40 and (b) low-heat concretes.

FIGURE 16: Cracking index in SV40 and low-heat concretes.

TABLE 6: Maximum stress and cracking risk index.

Concrete	Tensile stress (MPa)	Maturity (hours)	Tensile strength (MPa)	Cracking index
SV40	3.58	406	3.70	0.97
Low-heat	2.19	533	2.91	0.75

In the current study, the measured total deformation in the dilation rig for SV40 concrete under variable temperature conditions with $T_{max} = 60°C$ (60°C series) was separated into AS and TD by two constant CTEs: 8.5×10^{-6} or $10.0 \times 10^{-6}/°C$, as shown in Figure 20. Due to the lack of the general model to separate AS and TD, the total deformation measured from 60°C series was used for the whole SV40 wall in the analysis. The analysis results showed that the difference between the induced stresses at 7 days is about 10% for two different CTEs, and the conclusion is that as long as the input of total deformation is correct, the induced stress is not significantly affected by different separations of AS and TD. When the total deformation under realistic temperature history is available, although the CTE of the concrete in the early ages varies during the hydration process, the second strategy appears to be more robust since the CTE does not vary as much as autogenous shrinkage.

In real structure, the temperature varies in different locations. In the dilation rig and TSTM tests, the
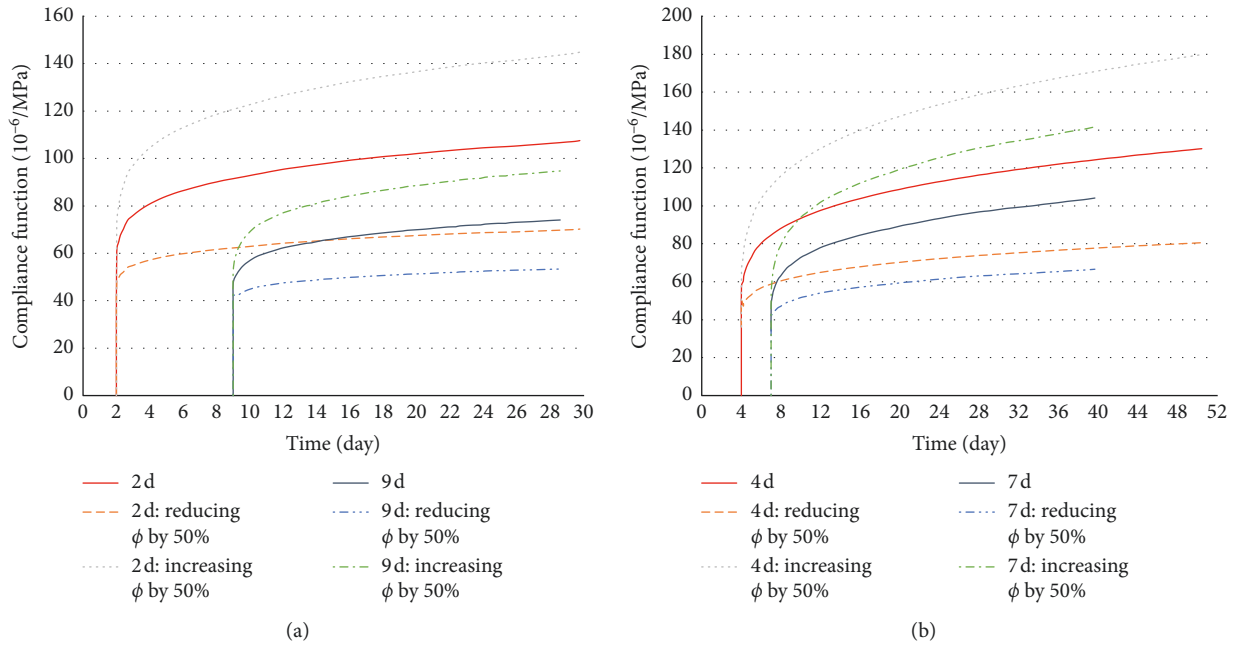
(a)

(b)

Figure 17: Compliance function with parameter φ reducing and increasing by 50%.

Table 7: Creep parameters.

Creep parameter	SV40			Low-heat		
	Test	+50%	−50%	Test	+50%	−50%
d		0.18			0.22	
p		0.18			0.26	
φ	1.10	1.65	0.55	1.60	2.40	0.80

(a)

(b)
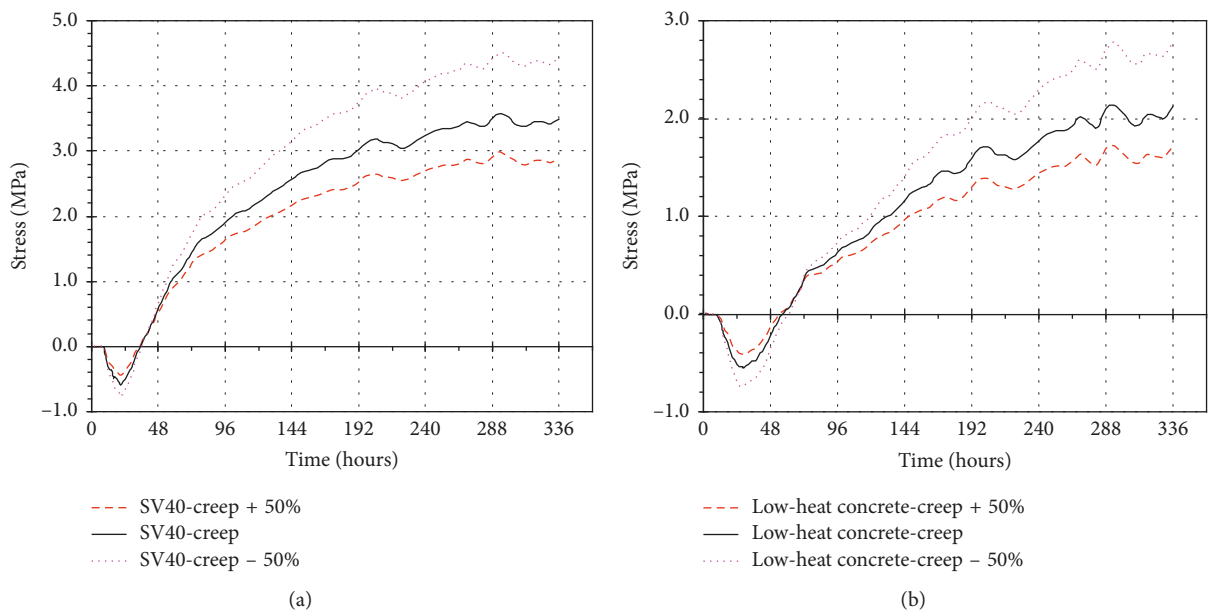
Figure 18: Calculated stress developments with 50% increase/decrease of parameter φ in creep compliance for (a) SV40 and (b) low-heat concretes.
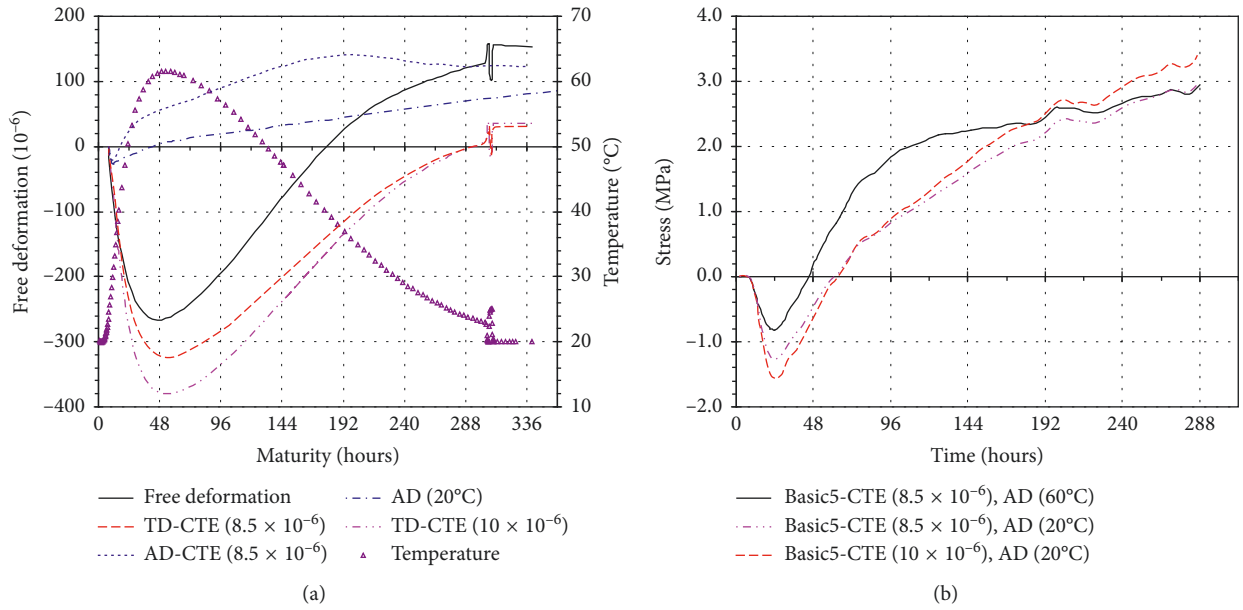
(a)

(b)

Figure 19: Different inputs of (a) total deformation and (b) stress development.
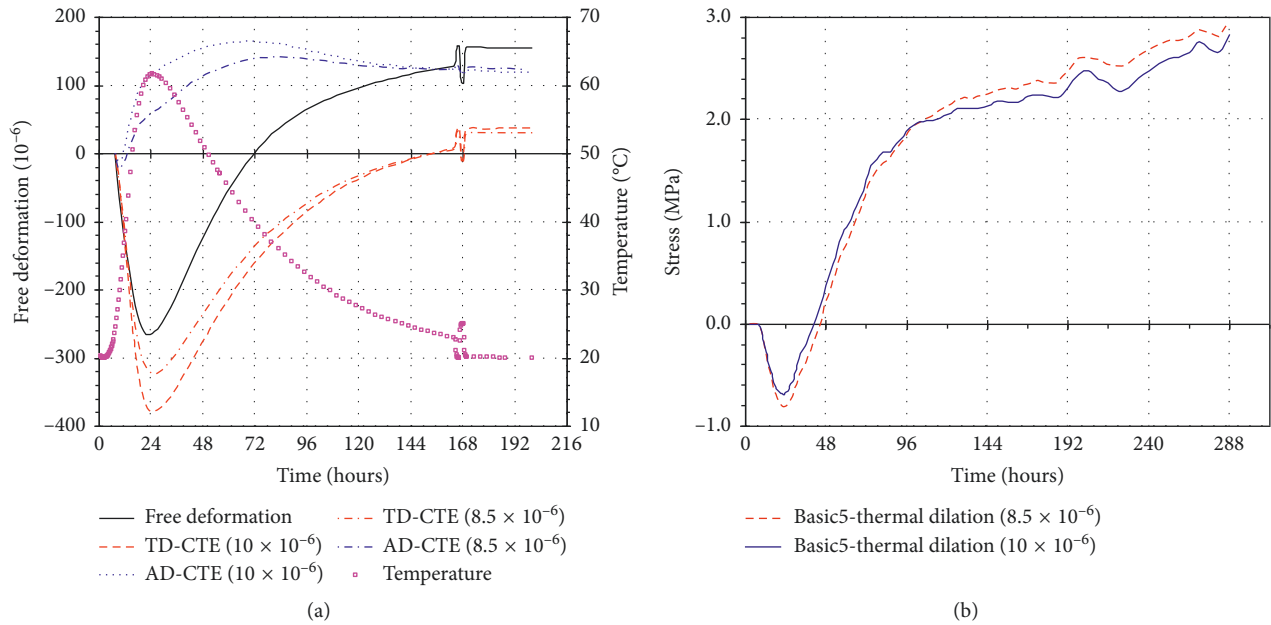

(a)

(b)

Figure 20: Different separations of (a) free deformation and (b) stress development.

Table 8: Autogenous shrinkage at different locations.

Location in wall	Applied autogenous shrinkage
Slice 1 and 5	29°C series (20°-29°-20°C temperature history)
Slice 2 and 4	47°C series (20°-47°-20°C temperature history)
Slice 3	60°C series (20°-60°-20°C temperature history)

temperature is approximately uniform in the specimen, and the improved procedure is to perform the dilation rig and TSTM tests under various temperature histories with different maximum temperatures and apply inputs of different total deformations in different temperature zones.

In the current study, the measured total deformations of SV40 concrete under variable temperature histories with the maximum temperatures of 29°C, 47°C, and 60°C, respectively, are separated into autogenous shrinkage and thermal dilation by constant CTE (8.5×10^{-6}/°C). The wall structure is sliced into five ranges, and the autogenous shrinkage under different temperature histories is used as the input for the different regions in the concrete wall, as shown in Table 8 and Figure 21.

The simulation result is compared with the case with only one autogenous shrinkage data from 60°C series which is applied in the whole wall. The stress development in the
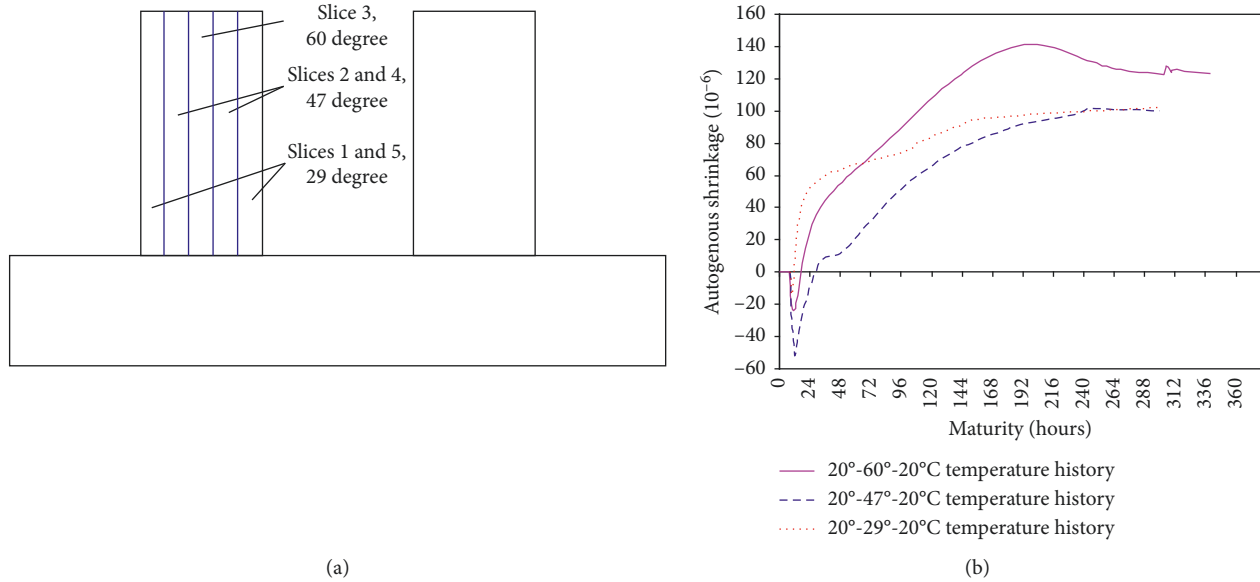
(a)

(b)

Figure 21: Different autogenous shrinkage inputs for different slices in the concrete wall.

middle slice of the wall is similar in those two cases, as shown in Figure 22, but the location of maximum tensile stress is different. For the case with different autogenous shrinkage inputs for different slices, the maximum tensile stresses occur in the second and fourth slices with autogenous shrinkage data from 47°C series. However, the maximum tensile stresses occur in the middle of the concrete wall for the cases with only one autogenous shrinkage data. The maximum tensile stress with different autogenous shrinkage inputs is 10% higher than that with one autogenous shrinkage input.

8. Conclusions

Based on well-documented material models, the numerical simulation could provide reasonably good prediction for the cracking risk of early age concrete. The calculated temperatures are in good agreement with the measured ones, and the deviation between calculated and measured maximum temperatures is in range of ±1.5°C for both SV40 and low-heat concretes. The calculated strains in the middle part of both walls (0.6–1.2 m above the slab) where the maximum stresses occur are in good agreement with the measured ones. This will ensure that the predicted crack indexes are reliable—as verified by the occurrence of severe cracks in SV40 concrete and fewer cracks in the low-heat concrete. The low-heat concrete with fly ash has a lower probability to crack under the given conditions, and replacement of cement with fly ash is beneficial in reducing cracking risk for young concrete.

Prediction of the crack index (or crack risk assessment in general) should be based on well-defined (measured) concrete properties, and the parameter study shows that creep has two opposite effects on tensile stress development in concrete. Creep in the early period decreases compressive stresses and consequently increases the tensile stress, while
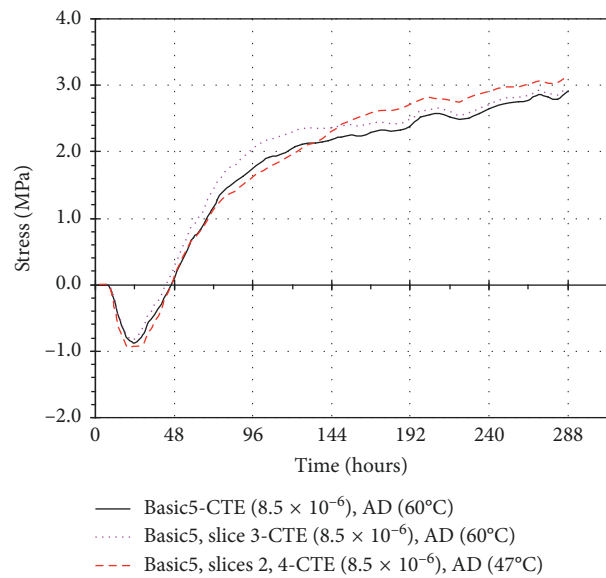

Figure 22: Stress developments in the concrete wall.

creep in the cooling period reduces tensile stresses. These two effects are competing, and in general, the latter effect prevails in most situations; the creep/relaxation properties significantly reduce the restraint stresses in concrete structure.

The volume changes of early age concrete is the driving force of the cracking risk, and the sum of thermal dilation and autogenous shrinkage can be measured in realistic temperature histories in the laboratory. As long as the total volume change is accurate, the separation of thermal dilation and autogenous shrinkage in different ways may not have significant influence on the simulated stress development in the hardening phase. When the volume changes are calculated by autogenous shrinkage measured under iso-thermal temperature conditions and assumed constant CTE,

one should be aware that this volume change may not be a close approximation for that in realistic temperature history because the temperature effect on autogenous shrinkage is quite uncertain especially under temperature histories with relatively high temperature. The use of measured volume changes under various temperature histories with different maximum temperatures, which closely represent the temperature distribution in the concrete structure, will give more reliable prediction of cracking risk in early age concrete structure.

Data Availability

The data used to support the findings of this study are available from the corresponding author upon request.
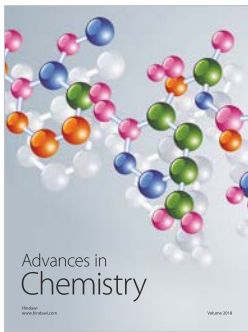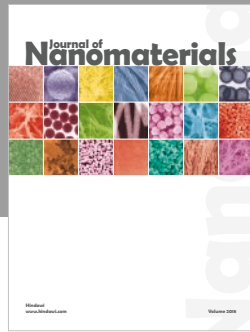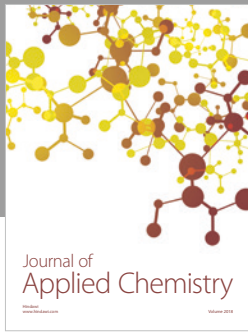
Conflicts of Interest

The authors declare that they have no conflicts of interest.

Acknowledgments

References

[1] S. Bernander and M. Emborg, "Risk of cracking in massive concrete structures—new development and experiences," *Thermal Cracking in Concrete at Early Ages*, R. Springenschmid, Ed., Proceeding of the RILEM International Symposium, pp. 385–392, E & FN Spon, London, UK, 1994.

[2] M. Emborg, "Development of mechanical behaviour at early ages," in *Prevention of Thermal Cracking in Concrete at Early Ages*, R. Springenschmid, Ed., pp. 77–148, E & FN Spon, London, UK, 1998.

[3] M. Emborg, "Thermal stresses in concrete structures at early ages," Ph.D. thesis, Luleå University of Technology, Luleå, Sweden, 1989.

[4] R. Springenschmidt, R. Breitenbucher, and M. Mangold, "Development of the cracking frame and temperature stresstesting machine," *Thermal Cracking in Concrete at Early-Age*, R. Springenschmid, Ed., pp. 137–144, E & FN Spon, London, UK, 1994.

[5] H. Hedlund, "Hardening concrete—measurement and evaluation of non-elastic deformation and associated restraint stresses," Ph.D. thesis, Division of Structural Engineering, Luleå University of Technology, Luleå, Sweden, 2000.

[6] A. B. E. Klausen, "Early age crack assessment of concrete structures: experimental determination of decisive parameters," Ph.D. thesis, NTNU, Trondheim, Norway, 2016, ISBN 978-82-326-1850-7.

[7] A. Knoppik-Wróbel and B. Klemczak, "Analysis of early-age thermal and shrinkage stresses in reinforced concrete walls," *ACI Structural Journal*, vol. 111, no. 2, pp. 313–322, 2014.

[8] A. K. Schindler, J. M. Ruiz, R. O. Rasmussen, G. K. Chang, and L. G. Wathne, "Concrete pavement temperature prediction and case studies with the FHWA HIPERPAV models,"

Cement and Concrete Composites, vol. 26, no. 5, pp. 463–471, 2004.

[9] N. Shi, Y. Chen, and Z. Li, "Crack Risk Evaluation of Early Age Concrete Based on the Distributed Optical Fiber Temperature Sensing," *Advances in Materials Science and Engineering*, vol. 2016, Article ID 4082926, 13 pages, 2016.

[10] G. M. Ji, "Cracking risk of concrete structures in the hardening phase: experiments, material modelling and finite element analysis," Ph.D. thesis, Deptartment of Structural Engineering, NTNU, Trondheim, Norway, 2008, ISBN 978-82-471-1079-9.

[11] G. M. Ji, T. Kanstad, and Ø. Bjøntegaard, "Calibration of material models against TSTM test for crack risk assessment of early age concrete containing fly ash," *Advances in Materials Science and Engineering*, vol. 2018, Article ID 1069181, 11 pages, 2018.

[12] *DIANA FEA User's Manual*, 2017.

[13] Z. P. Bažant, *Finite Element Analysis of Reinforced Concrete*, ASCE, New York, NY, USA, 1982.

[14] D. Bosnjak, "Self-induced cracking problems in hardening concrete structure," Ph.D. thesis, Department of Structural Engineering, NTNU, Trondheim, Norway, 2001, ISBN 82-7984-151-2.

[15] B. Klemczak and A. Knoppik-Wróbel, "Reinforced concrete tank walls and bridge abutments: early-age behaviour, analytic approaches and numerical models," *Engineering Structures*, vol. 84, pp. 233–251, 2014.

[16] T. Tanabe, M. Kawasurni, and Y. Yamashita, "Thermal stress analysis of massive concrete," in *Seminar Proceedings for Finite Element Analysis of Reinforced Concrete Structures*, ASCE, Tokyo, Japan, 21–24 May 1985.

[17] G. M. Ji, T. Kanstad, and Ø. Bjøntegaard, "Analysis of the SVV double wall field test related to the Bjørvika tunnel project," Tech. Rep. R-7-04, NTNU, Trondheim, Norway, 2004.

[18] J. E. Bowles, *Foundation Analysis and Design*, McGraw-Hill, San Francisco, CA, USA, 4th edition, 1988.

[19] P. Freiesleben Hansen and J. Pedersen, "Maturity computer for controlled curing and hardening of concrete," *Nordisk Betong*, vol. 1, pp. 19–34, 1977.

[20] T. Kanstad, T. A. Hammer, Ø. Bjøntegaard, and E. J. Sellevold, "Mechanical properties of young concrete: Part 1: experimental results related to test method and temperature effects," *Materials and Structures*, vol. 36, no. 4, pp. 218–225, 2003.

[21] T. Kanstad, T. A. Hammer, Ø. Bjøntegaard, and E. J. Sellevold, "Mechanical properties of young concrete: Part 2: determination of model parameters and test program proposals," *Materials and Structures*, vol. 36, no. 4, pp. 226–230, 2003.

[22] Z. P. Bažant and J. C. Chern, "Concrete creep at variable humidity," *Journal of Engineering Mechanics*, vol. 18, no. 103, 1985.

[23] Z. P. Bažant and J. C. Chern, "Concrete creep at variable humidity: constitutive law and mechanism," *Materials and Structures (RILEM)*, vol. 18, no. 1, pp. 1–20, 1985.

[24] M. Azenha, R. Faria, and D. Ferreira, "Identification of early-age concrete temperatures and strains: monitoring and numerical simulation," *Cement and Concrete Composites*, vol. 31, no. 6, pp. 369–378, 2009.

[25] Ø. Bjøntegaard, "Thermal dilation and autogenous deformation as driving force to self-induced stresses in high performance concrete," Ph.D. thesis, Department of Structural Engineering, NTNU, Trondheim, Norway, 1999, ISBN 82-7984-002-8.